Quantum signatures of the mixed classical phase space for three interacting particles in a circular trap

D. J. Papoular* and B. Zumer

Laboratoire de Physique Théorique et Modélisation, CNRS UMR 8089, CY Cergy Paris Université, 95302 Cergy-Pontoise, France

(Received 29 April 2024; accepted 3 July 2024; published 30 July 2024)

We study theoretically two consequences of the mixed classical phase space for three repulsively interacting bosonic particles in a circular trap. First, we show that the energy levels of the corresponding quantum system are well described by a Berry-Robnik distribution. Second, we identify stationary quantum states whose density is enhanced along the stable classical periodic trajectories, and calculate their energies and wave functions using the semiclassical Einstein-Brillouin-Keller (EBK) theory. Our EBK results are in excellent agreement with our full-fledged finite-element numerics. We discuss the impact of discrete symmetries, including bosonic exchange symmetry, on these classically localized states. They are within experimental reach, and occur in the same range of energies as the quantum scar reported in our previous work [Phys. Rev. A **107**, 022217 (2023)].

DOI: 10.1103/PhysRevA.110.012230

I. INTRODUCTION

The suppression of ergodicity in quantum systems has long been under intense scrutiny [1, Chap. 8], and atomic systems are very well suited to its investigation [2, Chap. 4]. The mechanisms leading to it in many-body systems, relying on, e.g., integrability [3], the presence of disorder [4], many-body scarring [5,6], or periodic driving [7], hold promise for quantum information processing over long times, but may hinder cooling mechanisms [8].

In the case of Hamiltonian systems, comparing the quantum system to its classical analog has been very fruitful in identifying such mechanisms [9]. Most classical systems have a mixed phase space hosting both ergodic and nonergodic trajectories. Ergodic trajectories densely cover a substantial fraction of the energy surface; nonergodic ones wind around tori found within the Kolmogorov-Arnold-Moser (KAM) regions of phase space, well described using KAM theory [10, Appendix 8]. Ergodicity in the quantum system may be suppressed in a phase space region corresponding to classical ergodic motion, e.g., by a quantum scar [11]. The quantum system is also known to exhibit regular levels reflecting the classical nonergodic trajectories [9, Sec. 4]. These levels may be studied using the semiclassical Einstein-Brillouin-Keller (EBK) theory [12,13]. In contrast to the semiclassical approaches applicable to the classically chaotic region, which mainly provide information concerning the density of states [14, Chap. 17], EBK theory applied to the classical KAM regions yields both quantum energy eigenvalues and eigenfunctions constructed from classically nonergodic trajectories. The full energy spectrum, including both the regular levels to which EBK theory applies and the remaining levels related to chaotic dynamics [9, Sec. 5], exhibits energy level statistics which significantly deviate [15,16] from both the Poisson and Wigner distributions respectively associated with classical integrability and chaos [14, Chap. 16].

Mixed classical phase spaces are relevant for the description of many-body systems. The many-body scar affecting the spin dynamics of a Rydberg atom chain observed in Ref. [5] provides a recent example. The classical analog system, whose construction is involved [17], exhibits mixed phase space, and KAM regions play a key role in the many-body quantum revivals [18]. Motivated by these recent developments, we introduced in our previous article [19] the system of three interacting particles in a circular trap. We analyzed this experimentally accessible system through well-established theories applied to a phase space whose dimension matches the number of independent parameters introduced in Ref. [18], and identified a quantum scar affecting the motion of the atoms.

In this paper, we analyze the role of its mixed classical phase space. First, we show that the parameters we investigated in Ref. [19] fall within a range where the quantum energy level statistics are well described by the Berry-Robnik distribution [16]. Then, we identify quantum states whose probability density is enhanced near stable classical periodic trajectories. Using EBK theory, we characterize their energy eigenvalues and explicitly construct their wave functions. Our results are in excellent agreement with our full-fledged numerical solution of the Schrödinger equation using the finite-element method. We highlight the role of discrete symmetries, including bosonic exchange symmetry, and their observable consequence, on the energies and wave functions of the considered localized states.

We formulate our analysis in terms of trapped Rydberg atoms, made accessible by recent experimental advances [20,21]. However, similar phenomena are expected to occur with systems of magnetic atoms [22] or polar molecules [23] exhibiting the same symmetries. The classically localized states [24, Chap. 22] identified in the present paper occur for the same parameters and energy range as

*Contact author: david.papoular@cyu.fr

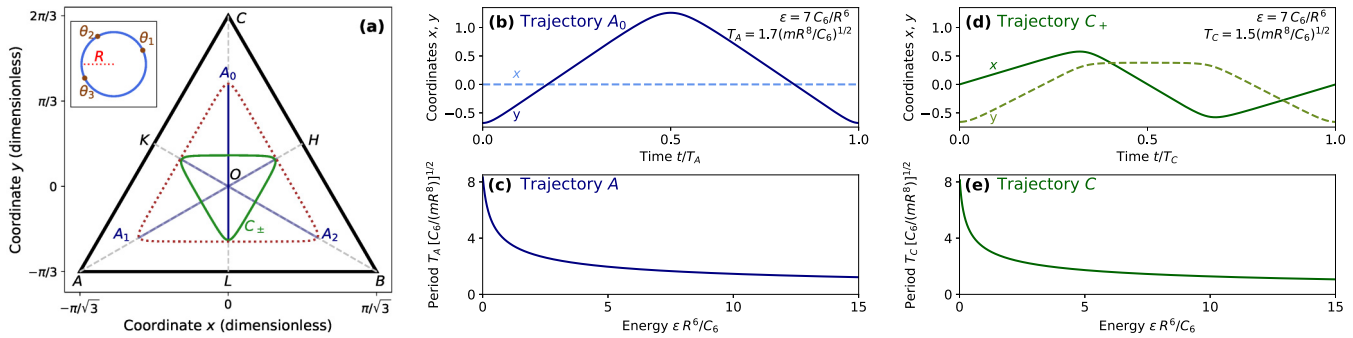

FIG. 1. (a) The periodic trajectories A_0, A_1, A_2 (straight blue lines) and C_+, C_- (the closed green trajectory is followed anticlockwise for C_+ and clockwise for C_-), shown in the (x, y) plane for the energy $\epsilon = 7C_6/R^6$. The dotted brown line shows the classically accessible region. The inset shows the considered physical system: three interacting particles in a circular trap. (b) Periodic trajectory A_0 as a function of time for $\epsilon = 7C_6/R^6$ in terms of its coordinates $x(t)$ (solid line) and $y(t)$ (dashed line). (c) Period $T_A(\epsilon)$ of trajectory A as a function of the energy ϵ. (d) and (e) show the corresponding quantities for trajectory C_+. Trajectories A and C are stable for the considered range of energies.

the previously identified quantum scar [19]. One may address one effect or the other simply by changing the initial condition defining the atomic motion. Hence, the simple, well-controlled atomic system we are proposing offers an opportunity for a detailed experimental comparison of the two effects.

The paper is organized as follows. In Sec. II, we introduce the considered system, and briefly summarize its properties described in detail in our previous article [19]. In Sec. III, we show that its quantum energy levels are well represented by the Berry-Robnik distribution. In Sec. IV, we apply EBK theory to identify the energy levels for the quantum states localized near stable periodic trajectories and construct the corresponding EBK wave functions, and we compare them to our finite-element numerical results. In Sec. V, we discuss experimental prospects. The article ends with the conclusive Sec. VI.

II. THE CONSIDERED SYSTEM

The system we analyze has been introduced in our previous article [19]. We briefly summarize its key features.

We consider three identical bosonic particles of mass m in a circular trap of radius R [Fig. 1(a), inset]. We assume that the interaction $v(d_{ij})$ between the particles i and j only depends on their distance $d_{ij} = 2R|\sin[(\theta_i - \theta_j)/2]|$. For circular Rydberg atoms whose electronic angular momenta are perpendicular to the plane, $v(d_{ij}) = C_6/d_{ij}^6$ with $C_6 > 0$. We introduce the Jacobi coordinates $x = [(\theta_1 + \theta_2)/2 - \theta_3 + \pi]/\sqrt{3}$, $y = (\theta_2 - \theta_1)/2 - \pi/3$, $z = (\theta_1 + \theta_2 + \theta_3)/3 - 2\pi/3$, and their conjugate momenta p_x, p_y, p_z (which carry the unit of action). Then, the Hamiltonian reads $H = p_z^2/(6mR^2) + H_{2D}$, where

$$H_{2D} = \frac{p_x^2 + p_y^2}{4mR^2} + V(x, y)\,. \tag{1}$$

Here, $V(x, y) = v(x, y)\,C_6/R^6$, with

$$v(x, y) = [\sin^{-6}(\pi/3 + y) + \sin^{-6}(\pi/3 + x\sqrt{3}/2 - y/2) + \sin^{-6}(\pi/3 - x\sqrt{3}/2 - y/2)]/64 - 1/9 \tag{2}$$

energies being measured from the minimum $V(\mathbf{0})$. The Hamiltonian H may be understood as describing either a classical system or its quantum counterpart. It is invariant under the point group C_{3v}, generated by the rotation of order 3 about the axis $(x = y = 0)$ and the reflection in the plane $(x = 0)$. The free motion of the coordinate z reflects the conservation of the total angular momentum p_z. Once the latter is fixed, the system is reduced to an effective point in the two-dimensional (2D) plane (x, y) within the equilateral triangle ABC of Fig. 1(a), in the presence of the potential $V(x, y)$.

From the quantum point of view, we seek the three-atom eigenstates of H in the form $\Psi_n(\theta_1, \theta_2, \theta_3) = \psi_n(\boldsymbol{r})\,e^{inz}$, where $\boldsymbol{r} = (x, y)$, and n is an integer setting the value of the quantized angular momentum p_z. The wave function $\psi_n(\boldsymbol{r})$ is fully determined by its values within the triangle ABC and vanishes along AB, BC, and CA. The constraint $\Psi_n(\theta_1, \theta_2, \theta_3) = \Psi_n(\theta_3 - 2\pi, \theta_1, \theta_2)$, combining bosonic symmetry and angular periodicity, yields

$$\psi_n(\mathcal{R}\boldsymbol{r}) = \psi_n(\boldsymbol{r})\,e^{2in\pi/3}\,, \tag{3}$$

where $\mathcal{R}$ is the rotation of angle $2\pi/3$ about O in the (x, y) plane. We sort the energy levels in terms of the three irreducible representations A_1, A_2, E of C_{3v}. Owing to Eq. (3), wave functions pertaining to the one-dimensional (1D) representations A_1 or A_2 have $n = 0$ modulo 3, whereas those pertaining to the 2D representation E have $n \neq 0$ modulo 3.

As in Ref. [19], we set the ratio $\eta = \hbar R^2/(mC_6)^{1/2}$ to 0.01, and we consider energies $\epsilon \sim 7C_6/R^6$.

III. MIXED CLASSICAL PHASE SPACE AND QUANTUM ENERGY LEVEL STATISTICS

A. Classical periodic trajectories

We have characterized the periodic trajectories of the model of Eq. (1) using our own C++ implementation of the numerical approach of Ref. [25]. We find three families of periodic trajectories existing for all energies $\epsilon > 0$: we label them A, B, C in analogy with those of the Hénon-Heiles potential [26]. We have analyzed the unstable trajectories of family B (i.e., their Lyapunov exponent >0), along with the quantum scar it yields, in our previous article [19]. By contrast, the

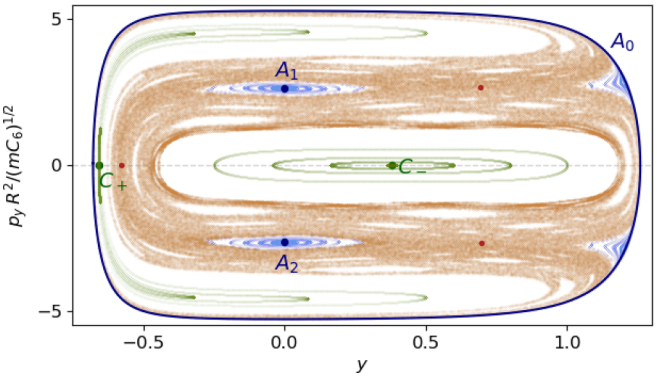

FIG. 2. Surface of section for Eq. (2), with $p_z = 0$, $\epsilon = 7C_6/R^6$, $x = 0$, and $p_x > 0$. The periodic trajectory A_0 appears as the dark blue closed boundary of the figure. All other periodic trajectories appear as fixed points, shown in dark blue for A_1 and A_2; dark red for B_1, B_2, and B_3; and dark green for C_+ and C_-. The stable trajectories A_i and C_j are surrounded by (light blue and light green) tori; no tori are present near the unstable trajectories B_k. The ≈287 000 thin brown dots all belong to the same ergodic trajectory.

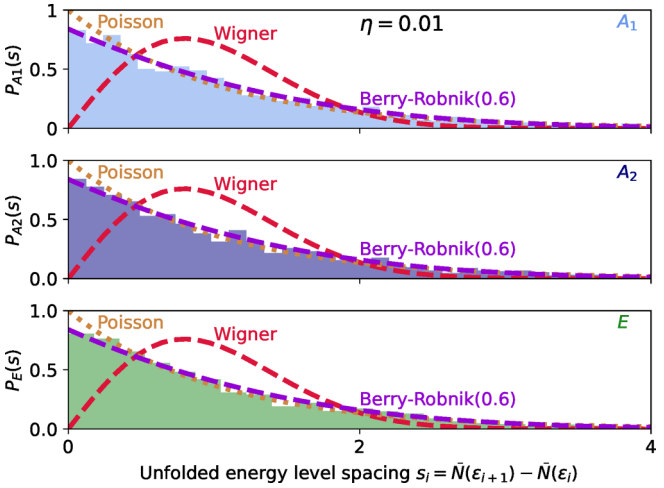

FIG. 3. The histograms show the distribution of unfolded energy level spacings $s_{r,i} = \bar{N}_r(\epsilon_i + 1) - \bar{N}_r(\epsilon_i)$ for states belonging to the three irreducible representations $r = A_1$ (top), A_2 (center), and E (bottom), which are analyzed separately. They differ from the Poisson (dotted golden line) and Wigner (dashed red line) distributions. They are well represented by the Berry-Robnik distribution, assuming a single chaotic region in phase space, with parameter $\rho_1 = 0.6$ for all three representations.

trajectories of families A and C are stable for all considered energies (i.e., their Lyapunov exponents = 0).

For a given energy ϵ, family A contains three straight-line trajectories A_0, A_1, A_2, which follow the medians of the triangular configuration space, and transform into one another under rotations of order 3. Family C contains two trajectories C_+ and C_-, which are closed loops around the center O: C_+ is followed anticlockwise and C_- clockwise, and they transform into each other under reflections about any of the three medians. All five trajectories are represented on the (x, y) plane in Fig. 1(a). The vertical trajectory A_0 and the trajectory C_+ are shown as functions of time on Figs. 1(b) and 1(d). Trajectories of a given family have the same period as a function of energy $T_A(\epsilon)$ and $T_C(\epsilon)$: these are plotted in Figs. 1(c) and 1(e) and are both of the order of $(mR^8/C_6)^{1/2}$ for $\epsilon \sim 7C_6/R^6$.

The simultaneous existence of stable and unstable periodic trajectories signals that the classical system represented by H_{2D} is neither integrable nor fully chaotic: its phase space is mixed. This is apparent on the surface of section of Fig. 2 [19]. There, the nonergodic trajectories are represented by the closed blue and green curves, which are sections in the two-dimensional plane of the KAM tori [10, Appendix 8] surrounding the stable trajectories A and C. We numerically find that the fraction of the surface of section not occupied by tori is densely covered by the intersections from a single ergodic trajectory, comprising the single ergodic zone visible on Fig. 2, within which lie the three unstable trajectories of family B.

B. Quantum energy level statistics

The quantum spectra of systems with mixed classical phase space satisfy neither the Poisson nor the Wigner distribution [14, Sec. 16.8]. We now verify this for the model of Eq. (2) and show that its energy level statistics are well represented by a Berry-Robnik distribution [16].

We numerically solve the Schrödinger equation for the Hamiltonian of Eq. (1) using the finite-element software FREEFEM [27]. We calculate stationary states belonging to the three irreducible representations A_1, A_2, E of the point group C_{3v} separately. We exploit discrete symmetries to reduce the configuration space to a triangle which slightly exceeds 1/6 of the classically accessible region for a given energy: details are given in our previous paper [19, Appendix 2]. We use a triangular mesh comprising 1000 vertices along each edge. We thus numerically obtain the energies and wave functions for slightly more than 1200 consecutive energy levels for Representation A_1, 1200 levels for Representation A_2, and 1700 nondegenerate levels for Representation E, in energy windows centered on $7C_6/R^6$.

For each irreducible representation $r = A_1$, A_2, and E of C_{3v}, we introduce the integrated density of states $N_r(\epsilon)$, which is the staircase-like function giving the number of stationary quantum states whose energies are smaller than ϵ [14, Sec. 16.2]. We describe its smooth component $\bar{N}_r(\epsilon)$ through its Weyl expansion, accounting for discrete symmetries [28]. We retain the leading-order term, proportional to $1/\hbar^2$, and the first correction, proportional to $1/\hbar$. We calculate the spacings $s_{r,i} = \bar{N}_r(\epsilon_i + 1) - \bar{N}_r(\epsilon_i)$ between consecutive "unfolded" energies $\bar{N}_r(\epsilon_i)$ [9, Sec. 5.4]. We plot their distribution on Fig. 3, where it is seen to differ from both the Poisson and the Wigner distributions [14, Secs. 16.3 and 16.4], as expected for a system with mixed classical phase space.

Figure 3 shows that the distribution of unfolded energy level spacings is well represented by the Berry-Robnik distribution [16], assuming that a single chaotic region in phase space contributes to the statistics, with the same parameter $\rho_1 = 0.6$ for all three representations. Both the assumption of a single chaotic region and the value $\rho_1 = 0.6$, representing the fraction of the energy surface over which motion is regular, are compatible with the surface of section of Fig. 2. The applicability of the Berry-Robnik distribution hinges on the

statistical independence of the regular and chaotic sequences of levels. Counterexamples have been identified, e.g., the hydrogen atom in a magnetic field [29], and its numerical verification with billiards requires reaching the deep semiclassical limit [30]. By contrast, our result provides a realization of the Berry-Robnik distribution in an experimentally accessible system involving smooth interatomic interactions rather than sharp billiard walls.

IV. QUANTUM STATIONARY STATES LOCALIZED NEAR THE CLASSICALLY STABLE PERIODIC TRAJECTORIES *A* AND *C*

For the majority of the stationary quantum states of the Hamiltonian H_{2D} that we have obtained numerically, the probability density $|\psi(x, y)|^2$ is not directly related to the periodic trajectories of types A and C. Nevertheless, we find multiple eigenstates whose probability density is enhanced along one or the other of these trajectories. Figures 6(a) and 6(b) and Figs. 7(a) and 7(b) illustrate this phenomenon for trajectories A and C, respectively: in each case, we show the probability density for the quantum states closest to the energy $\epsilon = 7C_6/R^6$. This phenomenon superficially resembles the quantum scars stemming from trajectory B, which we have identified in our previous article [19]. However, the quantum states we consider in the present article do not satisfy Heller's definition for a quantum scar [24, Chap. 22]. Indeed, in stark contrast to the classically unstable trajectory B, trajectories A and C are both classically stable. Hence, quantum mechanics yields no qualitative change in the behavior of the system in their vicinity. In this section, we illustrate this statement with two results. First, calculating the energies of the quantum states related to trajectories A and C semiclassically, we justify that they obey selection rules, which we entirely explain in terms of the symmetries of the classical KAM tori. Second, we construct semiclassical wave functions for these quantum states. Our semiclassical results for both the energies and the wave functions are in excellent agreement with our full quantum calculation.

A. Symmetries of the regular classical trajectories

We first consider the regular classical trajectories in the KAM regions of phase space surrounding the stable periodic trajectories of families A and C. Our numerical results show that the tori lying close to the periodic trajectories inherit the discrete symmetry properties of the corresponding periodic trajectories, namely, (1) a torus T_A near the periodic trajectory of type A invariant under the reflection $\mathcal{S}$ exhibits reflection symmetry, i.e., if the point $(\boldsymbol{r}, \boldsymbol{p})$ belongs to T_A, then so does $(\mathcal{S}\boldsymbol{r}, \mathcal{S}\boldsymbol{p})$; and (2) a torus T_C near a periodic trajectory of type C is invariant under rotations $\mathcal{R}$ of order 3, i.e., if the point $(\boldsymbol{r}, \boldsymbol{p})$ belongs to T_C, then so does $(\mathcal{R}\boldsymbol{r}, \mathcal{R}\boldsymbol{p})$.

We justify properties (1) and (2) through the following argument. We rely on an approximation introduced in Sec. 4.1 of Ref. [9]: we ignore narrow instability subregions and approximate the whole KAM region by a set of concentric tori. Our numerical results for the surface of section, shown on Fig. 2, confirm that it is very well satisfied for the inner tori, close to the periodic trajectories, which are of interest in this work (it breaks down for the outer tori in the vicinity of the ergodic zone, which we do not consider). This allows for the introduction of local action-angle coordinates, valid within this region. These are defined through the consistent choice of fundamental frequencies $\boldsymbol{\omega} = (\omega_1, \omega_2)$ [31, Sec. III.E] on each torus within the region. Then, any conditionally periodic trajectory $[\boldsymbol{r}(t), \boldsymbol{p}(t)]$ winding around one such torus may be written as a Fourier series [32, Sec. 52]:

$$\boldsymbol{r}(t) = \sum_{\boldsymbol{k}} \boldsymbol{r}_{\boldsymbol{k}} \exp(i\boldsymbol{k} \cdot \boldsymbol{\omega} t), \quad \boldsymbol{p}(t) = 2mR^2 d\boldsymbol{r}/dt \ , \tag{4}$$

the sum being taken over all integer pairs $\boldsymbol{k} = (k_1, k_2)$. The considered torus is uniquely determined by its actions $\boldsymbol{J} = (J_1, J_2)$, which are given by [33]

$$J_\alpha = \sum_{\alpha'=1,2} \sum_{\boldsymbol{k}} k_\alpha |\boldsymbol{r}_{\boldsymbol{k}}|^2 k_{\alpha'} \omega_{\alpha'} \ . \tag{5}$$

Let us justify statement (2), concerning tori in the vicinity of a periodic trajectory of type C. We consider a point $(\boldsymbol{r}, \boldsymbol{p})$ belonging to the KAM region surrounding trajectory C_+, and the rotated point $(\boldsymbol{r}', \boldsymbol{p}')$ with $\boldsymbol{r}' = \mathcal{R}_{2\pi/3}\boldsymbol{r}$ and $\boldsymbol{p}' = \mathcal{R}_{2\pi/3}\boldsymbol{p}$. Trajectory C_+ is invariant under rotations of order 3, so that $(\boldsymbol{r}', \boldsymbol{p}')$ also belongs to the same KAM region. We compare the two trajectories $[\boldsymbol{q}(t), \boldsymbol{p}(t)]$ and $[\boldsymbol{q}'(t), \boldsymbol{p}'(t)]$ obtained from the initial conditions $(\boldsymbol{r}, \boldsymbol{p})$ and $(\boldsymbol{r}', \boldsymbol{p}')$. Their Fourier components $\boldsymbol{r}_{\boldsymbol{k}}$ and $\boldsymbol{r}'_{\boldsymbol{k}}$, defined by Eq. (4), satisfy $\boldsymbol{r}'_{\boldsymbol{k}} = \mathcal{R}_{2\pi/3}\boldsymbol{r}_{\boldsymbol{k}}$, so that $|\boldsymbol{r}'_{\boldsymbol{k}}| = |\boldsymbol{r}_{\boldsymbol{k}}|$. According to Eq. (5), the actions J_α only depend on the modulus $|\boldsymbol{r}_{\boldsymbol{k}}|$, hence, they are the same for both trajectories. Therefore, the points $(\boldsymbol{r}, \boldsymbol{p})$ and $(\boldsymbol{r}', \boldsymbol{p}')$ belong to the same torus T_{C_+}. Statement (1) may be justified similarly.

B. EBK quantization: Energy levels

In this section, we obtain semiclassical predictions for the energies of the quantum levels related to trajectories A and C, which are in excellent agreement with the values obtained through our numerical solution of the Schrödinger equation [see Figs. 4(b) and 5(c)]. We also explain quasidegeneracies and derive selection rules, both of which are direct consequences of the discrete symmetries of the KAM tori presented in Sec. IV A above.

Our semiclassical description relies on EBK theory [12], accounting for the Maslov phase corrections [34, Sec. 7]. This theory generalizes the Wentzel-Kramers-Brillouin (WKB) approach [35, Sec. 48] to the quantization of regular classical motion with more than one degree of freedom [13]. We use our own implementation as a PYTHON script of the EBK approach, based on Refs. [31,36], which hinges on the representation of conditionally periodic motion in terms of the Fourier series of Eq. (4). We integrate classical trajectories over time intervals of lengths up to $t_{\max} = 3700(mR^8/C_6)^{1/2}$ and keep up to 3200 terms in Eq. (4).

We now characterize the quantum stationary states localized near the classically stable trajectories A and C. In Secs. IV B 1 and IV B 2 below, we derive the EBK energies for these states, considered as eigenstates of H_{2D}, whose wave functions depend on $\boldsymbol{r} = (x, y)$. In Sec. IV B 3, we analyze the role of angular momentum so as to discuss the stationary states of the three-particle Hamiltonian H, whose wave functions depend on (x, y, z).

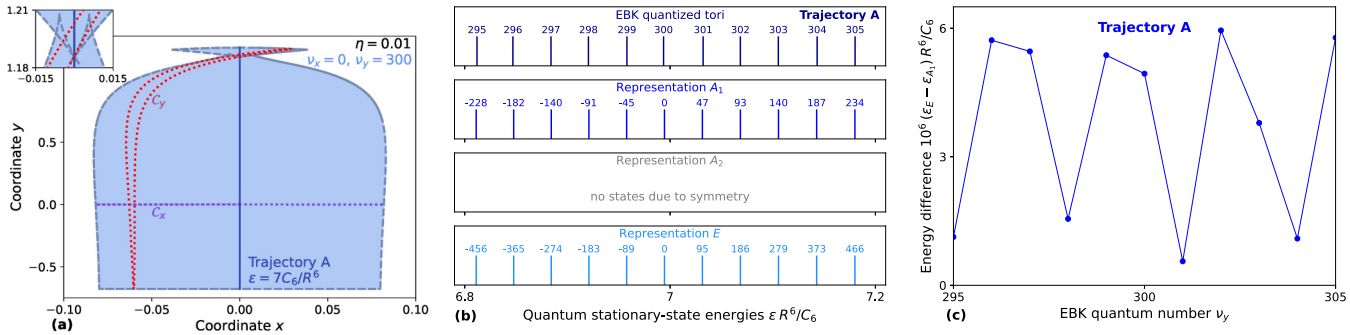

FIG. 4. (a) Classical trajectory A (solid dark blue) for the energy $\epsilon = 7C_6/R^6$, the nearest-energy trajectory satisfying Eq. (6) for $\eta = 0.01$ (densely covering the light blue area), and two independent circuits $\mathcal{C}_x$ (dotted purple) and $\mathcal{C}_y$ (dotted red) circling the torus, in terms of which the quantum numbers are $\nu_x = 0$ and $\nu_y = 300$. The dashed gray lines show the caustics of this trajectory. The top left inset zooms in on the narrow region near $(x = 0, y = 1.2)$ to reveal the self-intersection of the caustics. (b) Top panel: energies of the EBK wave functions for $\nu_x = 0$ and $295 \leqslant \nu_y \leqslant 305$. Center and bottom panels: energies of the corresponding quasidegenerate quantum stationary states belonging to representations A_1 (center) and E (bottom), obtained through our finite-element numerical calculations. Because of the torus symmetries, there are no states in representation A_2 corresponding to the EBK quantum numbers $(\nu_x = 0, \nu_y)$. The integers in the center and bottom panels specify the relative state indices within each representation, $\Delta\nu^{A_1}$ and $\Delta\nu^E/2$, with respect to the quantum state related to trajectory A, whose energy is closest to $7C_6/R^6$. (c) Small energy differences between the quasidegenerate states of representations A_1 and E.

1. Quantum states localized near trajectory A

For a given energy ϵ, the three periodic trajectories A_0, A_1, and A_2 [see Fig. 1(a)] and the tori surrounding them are mapped one onto the other through the rotations $\mathcal{R}$ and $\mathcal{R}^{-1}$. Hence, we focus on the vertical trajectory A_0. In Eq. (4), we choose the fundamental frequencies $\boldsymbol{\omega} = (\omega_1, \omega_2)$ as in Ref. [31, Fig. 8(b)]. This leads to the independent circuits $\mathcal{C}_x$ and $\mathcal{C}_y$ on Fig. 4(a). Calculating their Maslov indices [13, Sec. II.C], we obtain the EBK quantization condition for the tori near trajectory A,

$$I_x = \hbar(\nu_x + 1/2) \text{ and } I_y = \hbar(\nu_y + 1)\,, \tag{6}$$

where $I_{x,y}$ are the action integrals for the circuits $\mathcal{C}_{x,y}$, $\hbar$ is the reduced Planck's constant, and the integers $\nu_{x,y} \geqslant 0$ are the EBK quantum numbers. The action $I_x \geqslant \hbar/2$, so that the periodic trajectory A_0 itself does not satisfy Eq. (6). The tori satisfying Eq. (6) which are closest to trajectory A_0 are those with $\nu_x = 0$: the corresponding energies within a window centered on $\epsilon = 7C_6/R^6$ are shown on the top line of Fig. 4(b). We compare them to the energies of the stationary quantum states of H_{2D} belonging to representations A_1 and E localized near the trajectories A_0, A_1, and A_2, obtained through our finite-element calculations [see Figs. 6(a) and 6(b)]. These are shown in Fig. 4(b), middle and bottom lines, and are in excellent agreement with the EBK results.

Figure 4(b) reveals that each EBK energy corresponds to quasidegenerate quantum states pertaining to representations A_1 and E. Furthermore, no quantum stationary states pertaining to representation A_2 exhibit density profiles similar to Figs. 6(a) and 6(b). Both of these properties follow from the

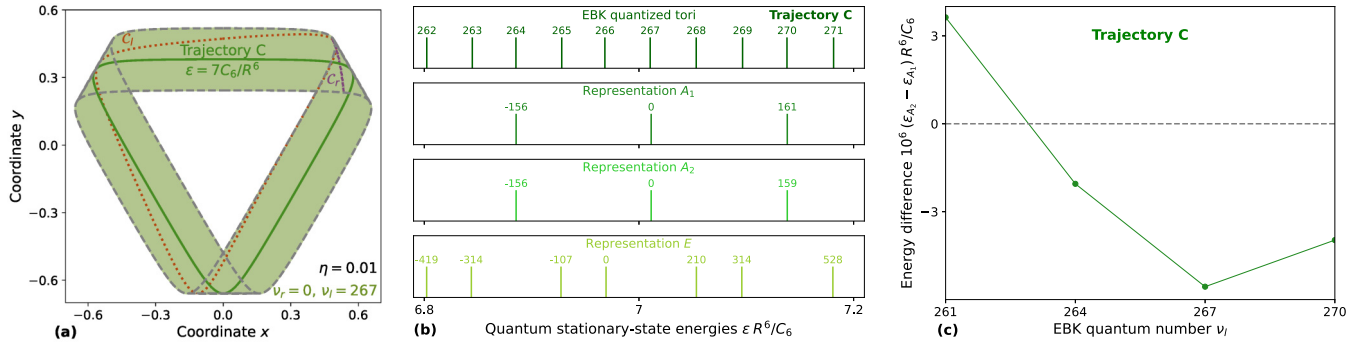

FIG. 5. (a) Classical trajectory C (solid dark green) for the energy $\epsilon = 7C_6/R^6$, the nearest-energy trajectory satisfying Eq. (9) for $\eta = 0.01$ (densely covering the light green area), and two independent circuits $\mathcal{C}_r$ (purple) and $\mathcal{C}_l$ (red) circling the torus, in terms of which the quantum numbers are $\nu_r = 0$, $\nu_l = 267$. The dashed gray lines show the caustics of this trajectory, which self-intersect in the top left, top right, and bottom regions. (b) Top panel: energies of the EBK wave functions for $\nu_r = 0$ and $262 \leqslant \nu_l \leqslant 271$. Three lower panels: energies of the corresponding quantum eigenstates belonging to representations A_1, A_2, and E, obtained through our finite-element numerical calculations. States in representations A_1 and A_2 exhibit quasidegeneracies and correspond to the EBK quantum numbers $\nu_r = 0$, $\nu_l = 0$ modulo 3; each EBK torus with quantum numbers $\nu_r = 0$, $\nu_l \neq 0$ modulo 3 yields two degenerate states in representation E. The integers specify the relative state indices within each representation, $\Delta\nu^{A_1}$, $\Delta\nu^{A_2}$, and $\Delta\nu^E/2$, with respect to the quantum state related to trajectory C whose energy is closest to $7C_6/R^6$. (c) Small energy differences between the quasidegenerate states of representations A_1 and A_2.

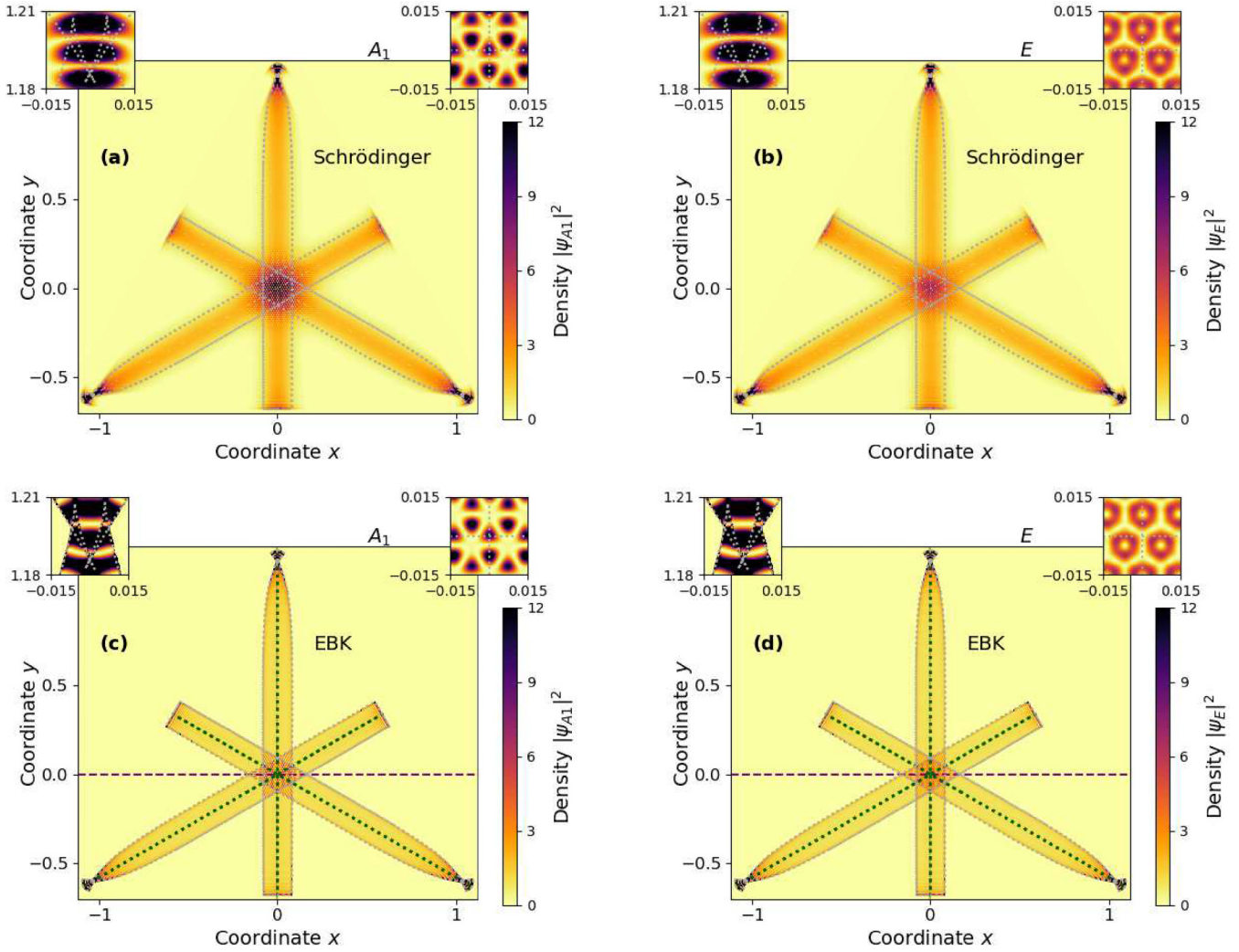

FIG. 6. Quantum states localized near the trajectories of family A. (a and b) Wave function densities $|\psi^{A_1}(\boldsymbol{r})|^2$ and $|\psi^{E}(\boldsymbol{r})|^2$ for the two quasidegenerate eigenstates of H_{2D} localized near the periodic trajectories of family A whose energies are closest to C_6/R^6, obtained through our finite-element numerical calculations. (c and d) The corresponding squared EBK wave functions $|\psi^{A_1}_{\mathrm{EBK}}(\boldsymbol{r})|^2$ and $|\psi^{E}_{\mathrm{EBK}}(\boldsymbol{r})|^2$, built from the KAM torus satisfying Eq. (6) with $\nu_x = 0$, $\nu_y = 300$ [see Fig. 4(a)]. On all four panels, the left inset details the region where the caustics self-intersect, and the right one shows the region near $(x = 0, y = 0)$.

symmetries of the regular trajectories identified in Sec. IV A above, through a mechanism identified in Refs. [37] and [9, Sec. 4.2] in the case where the discrete symmetry at play had order 2. The system we consider provides examples of the same phenomenon involving C_{3v} symmetry, as we now show.

We consider the EBK wave function $\psi_{\mathrm{EBK}}(\boldsymbol{r})$, corresponding to a torus in the vicinity of trajectory A_0, with the energy ϵ_{EBK}, satisfying Eq. (6) with $\nu_x = 0$. This torus is invariant under the reflection $\mathcal{S}$ about the vertical axis $x = 0$. Therefore, as shown in Ref. [9, Sec. 4.2],

$$\psi_{\mathrm{EBK}}(\mathcal{S}\boldsymbol{r}) = (-1)^{\nu_x}\psi_{\mathrm{EBK}}(\boldsymbol{r}) = \psi_{\mathrm{EBK}}(\boldsymbol{r})\,. \tag{7}$$

The EBK wave function ψ_{EBK} reflects the symmetry of the corresponding classical torus, but does not automatically satisfy the symmetry requirements of any representation. We now project it onto the irreducible representations [35, Sec. 94] A_1, A_2, and E. This yields three linearly independent wave functions, $\psi^{A_1}_{\mathrm{EBK}}$ and $\psi^{E,\pm}_{\mathrm{EBK}}$, pertaining to the representations A_1 and E, corresponding to the same semiclassical energy. In terms of kets $|\psi\rangle$, with $\langle\boldsymbol{r}|\mathcal{R}|\psi\rangle = \psi(\mathcal{R}^{-1}\boldsymbol{r})$ and $\langle\boldsymbol{r}|\mathcal{S}|\psi\rangle = \psi(\mathcal{S}\boldsymbol{r})$, they read

$$\begin{aligned}
\left|\psi^{A_1}_{\mathrm{EBK}}\right\rangle &= \alpha_{A_1}(1+\mathcal{R}+\mathcal{R}^{-1})\,|\psi_{\mathrm{EBK}}\rangle\,,\\
\left|\psi^{E,+}_{\mathrm{EBK}}\right\rangle &= \alpha_{E}(1+j^*\,\mathcal{R}+j\,\mathcal{R}^{-1})\,|\psi_{\mathrm{EBK}}\rangle\,,\\
\left|\psi^{E,-}_{\mathrm{EBK}}\right\rangle &= \alpha_{E}(1+j\,\mathcal{R}+j^*\,\mathcal{R}^{-1})\,|\psi_{\mathrm{EBK}}\rangle\,.
\end{aligned} \tag{8}$$

In Eq. (8), $\alpha_{A_1,E}$ are normalization coefficients, and $j = e^{2i\pi/3}$. We have used the relations $\mathcal{S}\mathcal{R}\mathcal{S} = \mathcal{R}^{-1}$ and Eq. (7). The states $|\psi^{A_1}_{\mathrm{EBK}}\rangle$ and $|\psi^{E,\pm}_{\mathrm{EBK}}\rangle$ satisfy $\mathcal{R}\,|\psi^{A_1}_{\mathrm{EBK}}\rangle = |\psi^{A_1}_{\mathrm{EBK}}\rangle$, $\mathcal{R}\,|\psi^{E,\pm}_{\mathrm{EBK}}\rangle = \pm j\,|\psi^{E,\pm}_{\mathrm{EBK}}\rangle$, and $|\psi^{E,-}_{\mathrm{EBK}}\rangle = \mathcal{S}\,|\psi^{E,+}_{\mathrm{EBK}}\rangle$. The component of ψ_{EBK} pertaining to representation A_2, proportional to $(1+\mathcal{R}+\mathcal{R}^{-1})(1-\mathcal{S})\,|\psi_{\mathrm{EBK}}\rangle$, is 0 because of Eq. (7).

2. *Quantum states localized near trajectory C*

We proceed as in Sec. IV B 1. For a given energy ϵ, the two periodic trajectories C_+ and C_- [see Fig. 1(a)] and

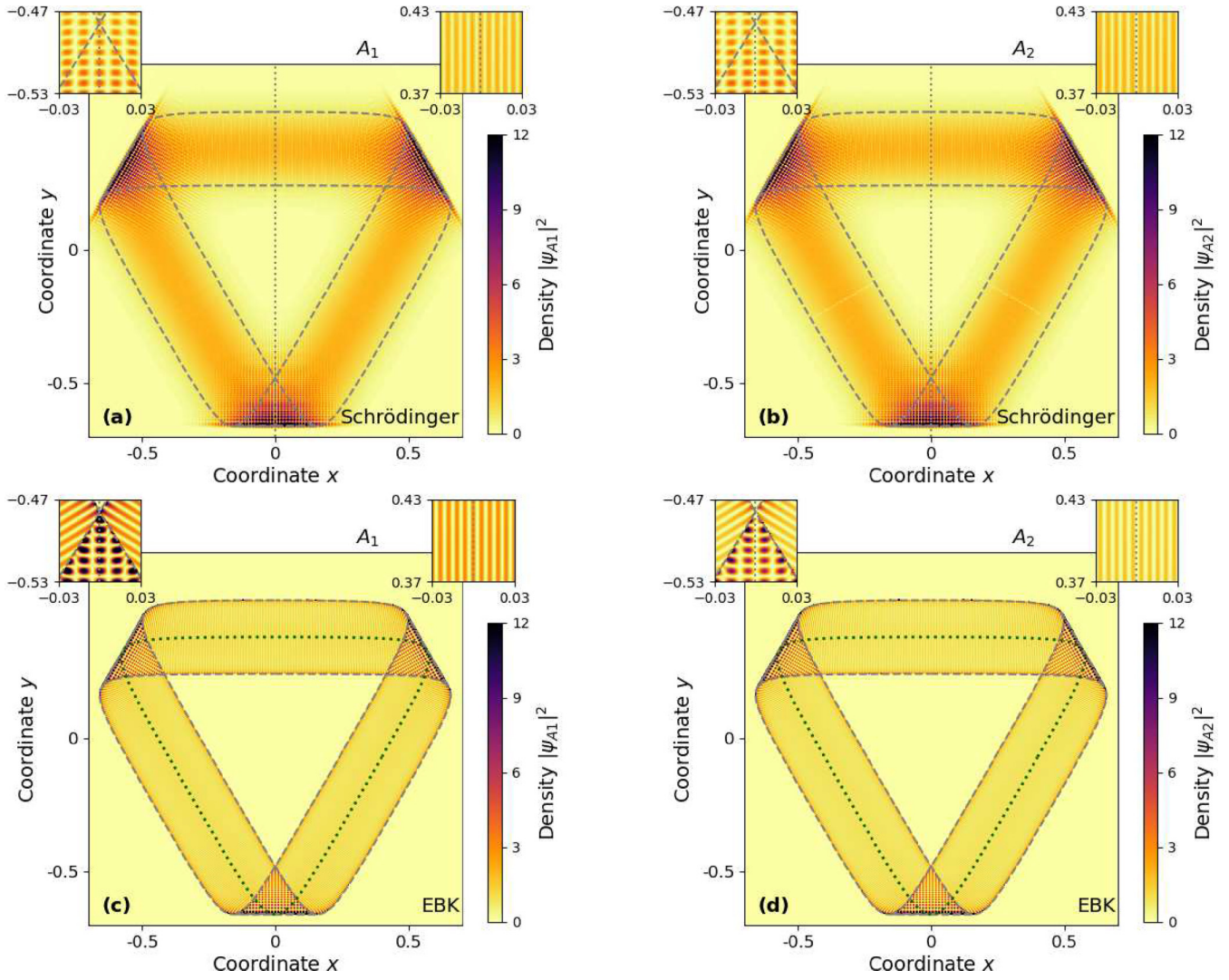

FIG. 7. Quantum states localized near the trajectories of family C. (a) and (b) Wave-function densities $|\chi^{A_1}(\boldsymbol{r})|^2$ and $|\chi^{A_2}(\boldsymbol{r})|^2$ for the two quasidegenerate eigenstates of H_{2D} localized near the periodic trajectories of family C whose energies are closest to C_6/R^6, obtained through our finite-element numerical calculations. (c) and (d) The corresponding squared EBK wave functions $|\chi^{A_1}_{\mathrm{EBK}}(\boldsymbol{r})|^2$ and $|\chi^{A_2}_{\mathrm{EBK}}(\boldsymbol{r})|^2$, built from the KAM torus satisfying Eq. (9) with $\nu_r = 0$ and $\nu_l = 267$ [see Fig. 5(a)]. On all four panels, the left inset details the region where the caustics self-intersect, and the right one shows the region near $(x = 0, y = 0.4)$.

the tori surrounding them are mapped onto each other through the reflection $\mathcal{S}$. Hence, we focus on the trajectory C_+. In Eq. (4), we choose the fundamental frequencies $\boldsymbol{\omega} = (\omega_1, \omega_2)$ as in Ref. [31, Fig. 8(a)], leading to the independent circuits $\mathcal{C}_r$ and $\mathcal{C}_l$ on Fig. 5(a). Calculating their Maslov indices, we obtain the EBK quantization condition for the tori near trajectory C,

$$I_r = \hbar(\nu_r + 1/2) \text{ and } I_l = \hbar(\nu_l + 1/2)\,, \tag{9}$$

where $I_{r,l}$ are the action integrals for the circuits $\mathcal{C}_{r,l}$, and the integers $\nu_{r,l} \geqslant 0$ are the EBK quantum numbers. The trajectory C_+ does not satisfy Eq. (9). The tori satisfying it which are closest to C_+ are those with $\nu_r = 0$; their energies are shown on the top line of Fig. 5(b). We compare them to the energies of the stationary quantum states of H_{2D} belonging to representations A_1, A_2, and E localized near the trajectories C_+ and C_-, obtained through our finite-element calculations [see Figs. 7(a) and 7(b)]. These are shown on the three lower lines of Fig. 5(b), and are in excellent agreement with the EBK results.

Figure 5(b) shows that each EBK energy with $\nu_r = 0$ and $\nu_l = 0$ modulo 3 corresponds to two quasidegenerate quantum states pertaining to representations A_1 and A_2. By contrast, each EBK energy with $\nu_r = 0$ and $\nu_l \neq 0$ modulo 3 corresponds to two exactly degenerate quantum states spanning a representation E. As for the states localized near trajectory A (see Sec. IV B 1 above), these properties follow from the symmetries of the regular trajectories (Sec. IV A). These are different from the symmetries of the tori surrounding trajectory A, leading to different selection rules, which we now derive.

We consider the EBK wave function $\chi_{\mathrm{EBK}}(\boldsymbol{r})$, corresponding to a torus in the vicinity of trajectory C_+, with the energy ϵ_{EBK}, satisfying Eq. (9) with $\nu_r = 0$. This torus is invariant under the rotation $\mathcal{R}$. A straightforward generalization of the argument in Ref. [9, Sec. 4.2] to symmetry operations of

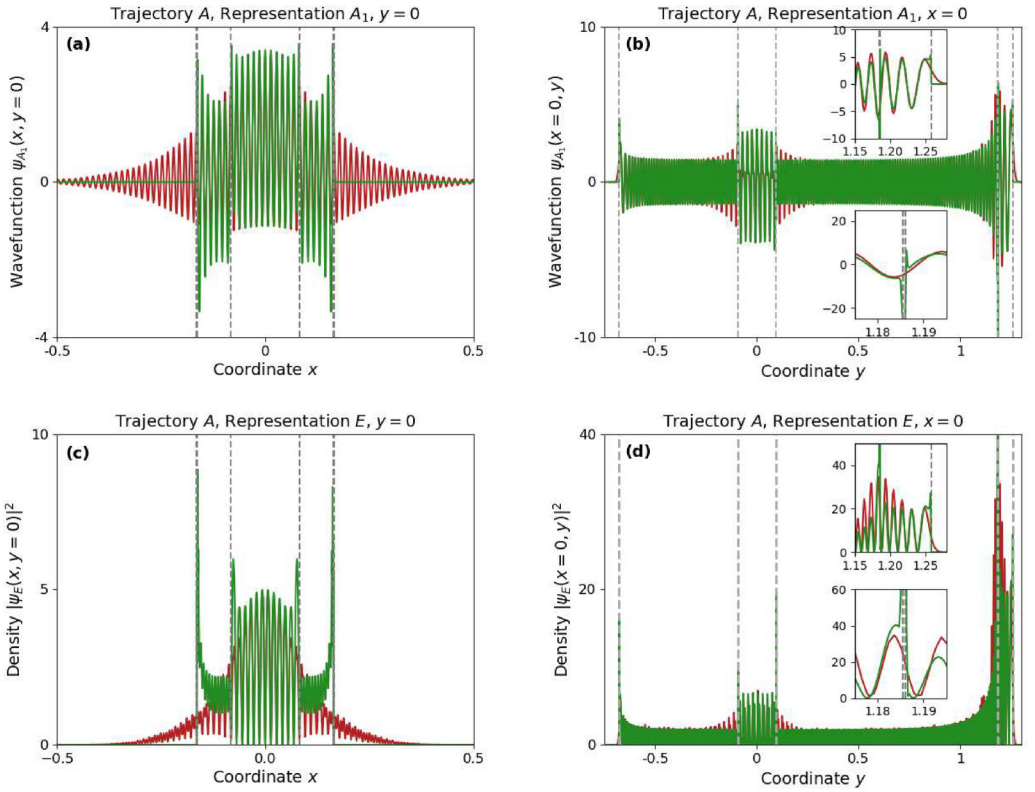

FIG. 8. Quantum states localized near the trajectories of family A. Comparison of the EBK (a) and (b) wave function $\psi^{A_1}_{\rm EBK}$ and (c) and (d) density $|\psi^{E}_{\rm EBK}|^2$ (green) with the corresponding quantities obtained through finite-element numerics (red) shown in Fig. 4, along the horizontal [(a) and (c)] and vertical [(b) and (d)] axes. The insets illustrate their behavior near the caustics (vertical dashed gray lines). Each EBK wave function has been scaled to match the finite-element wave function at the point $(x = 0, y = 0.5)$.

order 3 leads to $\chi_{\rm EBK}(\mathcal{R}\boldsymbol{r}) = j^{\nu_l}\,\chi_{\rm EBK}(\boldsymbol{r})$. We now project $\chi_{\rm EBK}$ onto the irreducible representations A_1, A_2, and E. For each ν_l, this yields two linearly independent, degenerate EBK wave functions. If $\nu_l = 0$ modulo 3, the nonvanishing wave functions pertain to representations A_1 and A_2:

$$\left|\chi^{A_1,A_2}_{\rm EBK}\right\rangle = \beta_{A_1,A_2}(1 \pm \mathcal{S})\,|\chi_{\rm EBK}\rangle\,, \tag{10}$$

with β_{A_1,A_2} being two normalization factors, whereas the component along E vanishes. By contrast, if $\nu_l \neq 0$ modulo 3, the components along A_1 and A_2 vanish, whereas the two nonvanishing wave functions $|\chi^{E,\pm}_{\rm EBK}\rangle$ span a representation E. For $\nu_l = -1$ modulo 3, $|\chi^{E,+}_{\rm EBK}\rangle = |\chi_{\rm EBK}\rangle$ and $|\chi^{E,-}_{\rm EBK}\rangle = \mathcal{S}\,|\chi_{\rm EBK}\rangle$, and the opposite assignment holds for $\nu_l = +1$ modulo 3.

3. *The role of angular momentum*

To discuss the three-particle eigenstates of H in terms of the eigenstates of $H_{\rm 2D}$ identified in Secs. IV B 1 and IV B 2, we now analyze the role of angular momentum.

We first consider quantum states localized near the periodic trajectories of family A. The two states $\psi^{E,\pm}_{\nu_y}(\boldsymbol{r})$ obtained for a given ν_y, are exactly degenerate eigenstates of $H_{\rm 2D}$ which span a 2D representation E. However, in terms of three-atom eigenstates of H, the states $\psi^{E,\pm}_{\nu_y}(\boldsymbol{r})e^{inz}$ occur if the total angular momentum $n = \mp 1$ modulo 3 because of Eq. (3).

The states $\psi^{A_1}_{\nu_y}(\boldsymbol{r})$ and $\psi^{E,\pm}_{\nu_y}(\boldsymbol{r})$ obtained for a given ν_y belong to different representations A_1 and E. Their quasidegeneracy is lifted by small couplings neglected in the EBK approach [9, Sec. 4.5], and the small energy difference is resolved in our finite-element numerical results, as shown in Fig. 4(c). Because of Eq. (3), the three-atom states $\psi^{A_1}_{\nu_y}(\boldsymbol{r})e^{inz}$ occur if $n = 0$ modulo 3, so that none of the three states $\psi^{A_1,E\pm}_{\nu_y}(\boldsymbol{r})e^{inz}$ may occur for the same value of n. They do not reduce to an EBK wave function corresponding to a single classical trajectory. Instead, Eq. (8) shows that they represent coherent superpositions of the three atoms undergoing motion near the trajectories A_0, A_1, and A_2.

We now turn to quantum states localized near the periodic trajectories of family C. The two states $\chi^{E,\pm}_{\nu_l}(\boldsymbol{r})$, obtained for a given $\nu_l \neq 0$ modulo 3, are exactly degenerate. The three-atom states $\chi^{E,\pm}_{\nu_l}(\boldsymbol{r})e^{inz}$ occur for $n = \mp 1$ modulo 3, and opposite values of n lead to atoms rotating along C in opposite directions. The two states $\chi^{A_1,A_2}_{\nu_l}(\boldsymbol{r})$ obtained for a given $\nu_l = 0$ modulo 3 belong to different representations and, hence, are quasidegenerate: their small energy difference is shown in Fig. 5(c). The three-atom states $\chi^{A_1,A_2}_{\nu_l}(\boldsymbol{r})e^{inz}$ may occur for the same value of $n = 0$ modulo 3.

C. EBK quantization: Wave functions

To further illustrate the applicability of the EBK approach to the quantum states localized near the stable periodic trajectories of families A and C, we construct primitive EBK wave functions for these states [38]. We focus on a given KAM torus satisfying the quantization conditions of either Eq. (6) or Eq. (9), depending on whether it lies near a trajectory

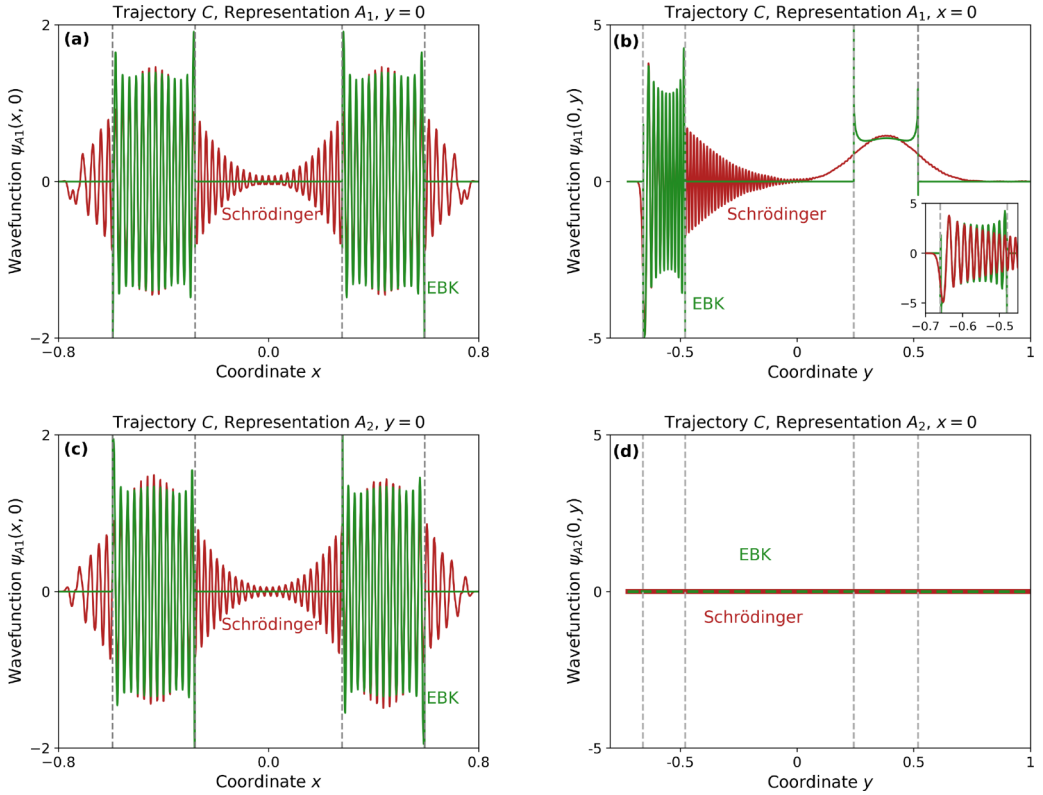

FIG. 9. Quantum states localized near the trajectories of family C. Comparison of the EBK wave functions (green) (a) and (b) $\chi_{\mathrm{EBK}}^{A_1}$ and (c) and (d) $\chi_{\mathrm{EBK}}^{A_2}$ and the corresponding wave functions obtained through finite-element numerics (red) shown in Fig. 5, along the horizontal [(a) and (c)] and vertical [(b) and (d)] axes. The insets illustrate their behavior near the caustics (vertical dashed gray lines). Each EBK wave function has been scaled to match the finite-element wave function at the point $(x = 0.5, y = 0)$.

of family A or C. To obtain the corresponding EBK wave functions ψ_{EBK} and χ_{EBK} of Secs. IV B 1 and IV B 2 above, the key extra required step with respect to the approach of Refs. [31,36] is to describe the torus in terms of multiple sheets on each of which the classical momentum is univalued [13, Sec. III.A]. These sheets join along the caustics of the classical trajectory in the (x, y) plane, shown as the dashed gray lines in Figs. 4(a) and 5(a). The caustics self-intersect, signaling the occurrence of catastrophes [39], and the torus sheetings must be constructed accordingly. We find that 12 sheets are required to describe tori near a trajectory of family A with $\nu_x = 0$, and that six sheets are required to describe tori near a trajectory of family C with $\nu_r = 0$. We then obtain the wave functions ψ_{EBK} and χ_{EBK} from the Fourier series of Eq. (4), in terms of linear superpositions of the contribution of each sheet [13, Sec. III.C]. Finally, we project ψ_{EBK} and χ_{EBK} onto the irreducible representations A_1, A_2, and E.

Figures 6(c) and 6(d) show the resulting EBK wave functions for the quasidegenerate quantum states $\psi^{A_1,E}(\boldsymbol{r})$ localized near the trajectories of family A whose energies are closest to $7C_6/R^6$. We compare them to the corresponding wave functions obtained through our finite-element numerical calculations [Figs. 6(a) and 6(b). We show the analogous results for the states $\chi^{A_1,A_2}(\boldsymbol{r})$, localized near the trajectories of family C, in Fig. 7. The agreement between the finite-element and EBK results is excellent, including in the catastrophe regions where the classical caustics self-intersect, shown in the upper left insets.

Primitive EBK wave functions do not account for the quantum penetration of the wave functions through the caustics. Instead, they diverge along the caustics as in the WKB approach [35, Sec. 46] and vanish outside the classical torus, as illustrated in Figs. 8 and 9 in the Appendix. This causes the two limitations of the EBK wave functions considered here. First, interference phenomena involving decaying waves outside the torus are not captured: the top left insets of Fig. 7 provide an example. Second, the divergence of the wave functions leads to numerical inaccuracies near the caustics which hinder their normalization. Hence, each of our EBK wave functions matches the finite-element wave function up to an overall normalization factor of order 2. We eliminate it by scaling the EBK wave function so that it matches the finite-element result at one single point chosen far from the caustics. The quantum penetration through the caustics may be accounted for, and hence both limitations be overcome, using a uniform approximation to the wave function [40, Sec. 7.2]. This goes beyond the scope of the present work.

V. EXPERIMENTAL PROSPECTS AND OUTLOOK

The effects considered here may be realized, e.g., on the system already considered in Ref. [19]: ^{87}Rb atoms in the circular Rydberg state $50C$, for which $C_6/h = 3\,\mathrm{GHz}\,\mu\mathrm{m}^6$. Then, the value $\eta = 0.01$ is achieved in a circular trap of radius $R = 7\,\mu\mathrm{m}$. The energy $\epsilon = 7C_6/R^6 = h \times 200\,\mathrm{kHz}$ is within experimental reach. For these parameters, the periodic

trajectories of families A, B, and C all have periods of the order of 1 ms. The position of the atoms may be detected at a given time by turning on a 2D optical lattice to freeze the dynamics, followed by atomic deexcitation and site-resolved ground state imaging. We focus on realizations where the total three-atom angular momentum n is well defined.

A key difference between the quantum scar of Ref. [19] and the localization near stable orbits considered here concerns the timescale over which quantum particles follow the classical periodic trajectories. For the quantum scar, the timescale over which quantum particles follow the classically unstable periodic trajectory is expected to depend on its inverse Lyapunov exponent [24, Chap. 22]. No such constraint exists for the dynamics near a classically stable orbit, so that recurrences of the initial state may be sought for over the lifetime of the trapped atoms.

Next, we point out a consequence of quantum coherence. According to Sec. IV B 3, the quantum states localized near the trajectories of family A are equal-weight superpositions of states localized near the three periodic trajectories of family A (rather than just one trajectory). This is the impact of bosonic symmetry. By contrast, motion along a single trajectory C_+ or C_- may be observed.

The following point warrants further investigation. Three atoms launched with angular momentum $n = 0$ modulo 3 near the periodic trajectory C_+ may undergo dynamical tunneling [41] to the trajectory C_-. The expected oscillation period, set by $h/(\epsilon_{\nu_l,A_2} - \epsilon_{\nu_l,A_1})$, is $\sim$25 s for the parameters of Fig. 5(c). This very long timescale is out of reach of current setups, but should become accessible in new experiments currently under construction promising atomic lifetimes $\sim$1 min [42,43]. Furthermore, the period may be minimized by varying the energy ϵ and the parameter η. Dynamical tunneling has already been observed for noninteracting, periodically driven atoms [44,45]. The system we consider would provide an example involving interacting atoms described by a time-independent Hamiltonian.

VI. CONCLUSION

We have revisited the system of three interacting bosonic particles in a circular trap that we had first considered in Ref. [19]. We have illustrated the mixed nature of its classical phase space, and shown that the statistics of the quantum levels are well described by a Berry-Robnik distribution. We have analyzed the symmetries of the quantum states localized along the classically stable periodic trajectories A and C, calculated their energies semiclassically using EBK theory, and constructed the corresponding EBK wave functions. Our semiclassical EBK results, regarding both the energies and the wave functions, are in excellent agreement with the quantum eigenstates and energies which we have obtained through finite-element numerical calculations. Thus, the considered system hosts both a quantum scar, analyzed in Ref. [19], and classical localization near stable periodic orbits, analyzed in the present work. These phenomena, all within experimental reach, occur in the same energy range: to observe one or the other, one simply adapts the initial conditions so as to launch the three atoms along a classical periodic orbit which is either unstable or stable. Hence, the system we propose appears promising in view of a detailed experimental comparison between quantum scars and classically localized states.

ACKNOWLEDGMENTS

We acknowledge stimulating discussions with M. Brune and J. M. Raimond (LKB, Collège de France), F. Dunlop (LPTM, Cergy-Pontoise), and R. J. Papoular (IRAMIS, CEA Saclay).

APPENDIX: COMPARISON BETWEEN SCHRÖDINGER AND EBK WAVE FUNCTIONS

The Supplemental Figs. 8 and 9 on the next page compare the behavior of the EBK wave functions to those obtained by solving the Schrödinger equation for the Hamiltonian H_{2D} through finite-element numerics along the horizontal and vertical axes. They show excellent agreement between the two approaches, and highlight the key limitation of the EBK wave functions: the quantum penetration through the caustics is not accounted for, and is replaced by a divergence along the caustics.

[1] F. Haake, S. Gnutzmann, and M. Kuś, *Quantum Signatures of Chaos*, 4th ed. (Springer, New York, 2018).
[2] H.-J. Stöckmann, *Quantum Chaos: An Introduction* (Cambridge University, Cambridge, 1999).
[3] X. Guan and P. He, Rep. Prog. Phys. **85**, 114001 (2022).
[4] D. A. Abanin, E. Altman, I. Bloch, and M. Serbyn, Rev. Mod. Phys. **91**, 021001 (2019).
[5] H. Bernien, S. Schwartz, A. Keesling, H. Levine, A. Omran, H. Pichler, S. Choi, A. S. Zibrov, M. Endres, M. Greiner, V. Vuletić, and M. D. Lukin, Nature (London) **551**, 579 (2017).
[6] C. J. Turner, A. A. Michailidis, D. A. Abanin, M. Serbyn, and Z. Papić, Nat. Phys. **14**, 745 (2018).
[7] D. Bluvstein, A. Omran, H. Levine, A. Keesling, G. Semeghini, S. Ebadi, T. T. Wang, A. A. Michailidis, N. Maskara, W. H. Ho, S. Choi, M. Serbyn, M. Greiner, V. Vuletić, and M. D. Lukin, Science **371**, 1355 (2021).
[8] M. Brune and D. J. Papoular, Phys. Rev. Res. **2**, 023014 (2020).
[9] O. Bohigas, S. Tomsovic, and D. Ullmo, Phys. Rep. **223**, 43 (1993).
[10] V. I. Arnold, *Mathematical Methods of Classical Mechanics*, 2nd ed. (Springer, New York, 1989).
[11] E. J. Heller, Phys. Rev. Lett. **53**, 1515 (1984).
[12] J. B. Keller, Ann. Phys. **4**, 180 (1958).
[13] I. C. Percival, Adv. Chem. Phys. **36**, 1 (1977).
[14] M. C. Gutzwiller, *Chaos in Classical and Quantum Mechanics* (Springer, New York, 1990).
[15] T. A. Brody, Lett. Nuovo Cimento **7**, 482 (1973).
[16] M. V. Berry and M. Robnik, J. Phys. A **17**, 2413 (1984).

[17] C. J. Turner, J.-Y. Desaules, K. Bull, and Z. Papić, Phys. Rev. X **11**, 021021 (2021).
[18] A. A. Michailidis, C. J. Turner, Z. Papić, D. A. Abanin, and M. Serbyn, Phys. Rev. X **10**, 011055 (2020).
[19] D. J. Papoular and B. Zumer, Phys. Rev. A **107**, 022217 (2023).
[20] R. G. Cortiñas, M. Favier, B. Ravon, P. Méhaignerie, Y. Machu, J. M. Raimond, C. Sayrin, and M. Brune, Phys. Rev. Lett. **124**, 123201 (2020).
[21] D. Barredo, V. Lienhard, P. Scholl, S. de Léséleuc, T. Boulier, A. Browaeys, and T. Lahaye, Phys. Rev. Lett. **124**, 023201 (2020).
[22] L. Chomaz, I. Ferrier-Barbut, F. Ferlaino, B. Laburthe-Tolra, B. L. Lev, and T. Pfau, Rep. Prog. Phys. **86**, 026401 (2023).
[23] J. L. Bohn, A. M. Rey, and J. Ye, Science **357**, 1002 (2017).
[24] E. J. Heller, *The Semiclassical Way to Dynamics and Spectroscopy* (Princeton University, Princeton, 2018).
[25] M. Baranger, K. T. R. Davies, and J. H. Mahoney, Ann. Phys. **186**, 95 (1988).
[26] K. T. R. Davies, T. E. Huston, and M. Baranger, Chaos **2**, 215 (1992).
[27] F. Hecht, J. Numer. Math. **20**, 251 (2012).
[28] B. Lauritzen and N. D. Whelan, Ann. Phys. **244**, 112 (1995).
[29] D. Wintgen and H. Friedrich, Phys. Rev. A **35**, 1464 (1987).
[30] T. Prosen, J. Phys. A **31**, 7023 (1998).
[31] C. C. Martens and G. S. Ezra, J. Chem. Phys. **86**, 279 (1987).
[32] L. D. Landau and E. M. Lifshitz, *Mechanics*, 3rd ed. (Butterworth Heinemann, Woburn, 1976).
[33] I. C. Percival, J. Phys. A **7**, 794 (1974).
[34] V. P. Maslov and M. V. Fedoriuk, *Semi-Classical Approximations in Quantum Mechanics* (Reidel, Dordrecht, 1981).
[35] L. D. Landau and E. M. Lifshitz, *Quantum Mechanics, Non-Relativistic Theory*, 3rd ed. (Butterworth Heinemann, Woburn, 1977).
[36] C. C. Martens and G. S. Ezra, J. Chem. Phys. **83**, 2990 (1985).
[37] J. G. Leopold, I. C. Percival, and D. Richards, J. Phys. A **15**, 805 (1982).
[38] S. K. Knudson, J. B. Delos, and D. W. Noid, J. Chem. Phys. **84**, 6886 (1986).
[39] J. B. Delos, J. Chem. Phys. **86**, 425 (1987).
[40] A. M. Ozorio de Almeida, *Hamiltonian Systems: Chaos and Quantization* (Cambridge University, Cambridge, 1988).
[41] S. Tomsovic, Phys. Scr. **T90**, 162 (2001).
[42] T. L. Nguyen, J. M. Raimond, C. Sayrin, R. Cortiñas, T. Cantat-Moltrecht, F. Assemat, I. Dotsenko, S. Gleyzes, S. Haroche, G. Roux, T. Jolicoeur, and M. Brune, Phys. Rev. X **8**, 011032 (2018).
[43] P. Méhaignerie, C. Sayrin, J. M. Raimond, M. Brune, and G. Roux, Phys. Rev. A **107**, 063106 (2023).
[44] W. K. Hensinger, H. Häffner, A. Browaeys, N. R. Heckenberg, K. Helmerson, C. McKenzie, G. J. Milburn, W. D. Phillips, S. L. Rolston, H. Rubinsztein-Dunlop, and B. Upcroft, Nature (London) **412**, 52 (2001).
[45] D. A. Steck, W. H. Oskay, and M. G. Raizen, Science **293**, 274 (2001).